Effect of solution flow rate on growth and characterization of nanostructured ZnO thin films deposited using spray pyrolysis

S. Zargou[1], S.M. Chabane Sari*[1], A.R. Senoudi[1], M. Aida[2], N. Attaf[2], I.F. Hakem[3]

[1]*Laboratory of Research on Macromolecules, Faculty of Sciences, University Abu Bekr Belkaïd, Tlemcen, Algeria.*
[2]*Thin Films and Interfaces Laboratory, Faculty of Science, University of Constantine 1, Algeria.*
[3]*Materials Science and Engineering Department, Carnegie Mellon University 5000 Forbes Avenue, Pittsburgh, PA 15213 USA.*

Abstract

ZnO thin films were grown from 60 ml of spray solution on glass substrates by chemical spray at 300°C using solution low spray rates of 5, 10, 15 and 20 ml/h. X-ray diffraction data showed films grow preferentially in the (100) plane parallel to the substrate, with average grain size ranged from 20.6 nm to 35.3 nm. The electrical resistivity of sprayed ZnO thin films is controlled by the solution spray rate, it decreases from $4.048 \times 10^3 \ \Omega$ cm to $0.781 \times 10^3 \ \Omega$ cm respectively when spray rate is increased from 5ml/h to 20 ml/h independent of the film thickness; Sprayed ZnO films transmit 97- 99 % of the visible light. The optical band gap energy is found to be direct allowed transition ~3.26 eV. At optimal solution spray rate S_f = 15 ml/h, the ZnO thin film exhibits low sheet resistance Rs = $5.25 \times 10^9 \ \Omega/\square$ and highest figure of merit Φ_{TC} = $17.4 \times 10^{-11} \ \Omega^{-1}$.

Keywords: ZnO thin films, Ultrasonic spray, XRD, Optical transmission, Electrical properties

1. Introduction

Zinc Oxide (ZnO) is one of the promising II-VI semi conducting materials for technological applications (such as micro and optoelectronics, sensors, surface acoustics wave devices and solar cells) and thus plays an important role in several areas of physics, chemistry and materials science. It has been widely studied and continues to receive considerable attention, due to its low cost, nontoxicity, high stability and high optical transparency in the visible and near infrared region [1- 6]. It has been well established that the optical and electronic properties of thin films are sensitive to minute variations in structural features that in turn sensitively depend on the fabrication conditions of thin film [7]. To improve ZnO properties, various growth techniques, including chemical vapor deposition [8], sol–gel method [9], electrochemical deposition [10], sputter deposition [11], hydrothermal technique [12] and spray pyrolysis technique (SPT) [13, 14] have been employed to obtain pure ZnO thin films on various substrates. SPT in particular has attracted attention due to its versatility, scalability and the possibility to control the thickness of thin films and hence tailor them to specific applications. The economic viability of SPT derives from the advantage of inexpensive equipment (non-vacuum method), the ease of large area deposition and continuous fabrication by moving nozzle over a substrate. To achieve good quality sprayed thin films with the desired product composition and morphology, understanding of the role of process parameters such as substrate temperature, spray rate, solution concentration and, pressure of the carrier gas on the product characteristics is crucial [15]. In SPT, spray rate (S_f) optimization is a crucial step because it governs the preferred orientation, structural, optical and electrical properties [16-18].

The objective of the present work is to contribute to the better understanding of the role of process parameters on the physical properties of ZnO films fabricated by SPT. In particular, ZnO thin films were fabricated using SPT with systematically varied solution flow rate to establish the role of S_f on the optical, electrical, structural properties of ZnO films and to identify process conditions to maximize the figure of merit (Φ_{TC}) of thin films.

2. **Experimental**

2.1. *Thin-film deposition*

Thin film deposition using the spray pyrolysis technique (SPT), involves spraying a metal salt solution onto a heated substrate [19, 20]. The Figure 1 shows schematic diagram of spray experimental used in deposition of the ZnO thin films [57]. Different solution flow rates were investigated as shown in Table 1. The precursor solution was prepared by dissolving 0.1 M of zinc acetate ($Zn(CH_3COO)_2$, $2H_2O$, purchased from Sigma-Aldrich, Germany and with a purity of 99.5%) salt in deionized water. Before deposition, the glass substrates were cleaned with methanol and deionized water. The distance between the nozzle and substrate was about 3 cm. The prepared solution was sprayed independently onto the clean glass substrates within a deposition time kept constant at 10 min to achieve ZnO films formation. In this procedure, the solution is sprayed in fine droplets by ultrasonic by ultrasonic generator 40KHz. which transforms the liquid to a stream formed with uniform and fine droplets of 40µm average diameter (given by the manufacturer). Compressed air was used to atomize the solution containing the precursor compounds through a spray nozzle over the heated substrate. The substrate holder was equipped with a thermocouple, heating element and temperature controller. The spray nozzle is specially designed with two concentric glass pipes. Through the inner pipe, flows the solution and between the inner and outer, the air stream; the spray is produced by the Venturi effect at the end of both pipes. As the precursor droplets arrive on the heated substrate, a thermochemical decomposition process occurs and high quality ZnO thin films were deposited on glass substrates. After fixing the precursor volume at 60 ml and substrate temperature at 300 °C in all cases, a series of thin films were deposited using four different flow rates namely, S_f = 5, 10, 15 and 20 ml/h.
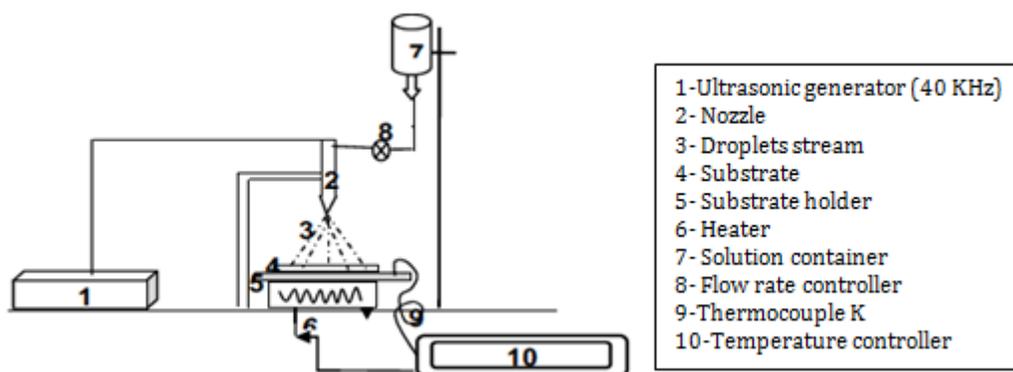
Figure 1: Schematic diagram of spray experimental setup [57]

2.2. *Characterization of ZnO thin film*

2.2.1 *Uv-visible measurements*

Spectral transmittance was measured with a Shimadzu UV-vis-NIR scanning spectrophotometer (UV-1301 PC spectrometer). Film thickness (d) was determined by counting the interference fringes formed on the sample by using the method described in reference [21]. However for small thicknesses (d ≤ 200 nm) no fringes of interference (required for calculating the thickness) were observed. Consequently, the ellipsometry technique with 632.8 nm laser source has been used.

Table 1: Optimized deposition parameters of 0.1 M precursor solution

Parameters	Values
ZnO Precursor	Zinc acetate dehydrate (S = 1316.94 mg)
Precursor molarity	0.1 M
Substrate temperature	573 °K
Atmosphere	Air
Solvent	Methanol (CH_3-OH)
Solution flow rate	S_f = 5ml/h; 10ml/h; 15ml/h; 20ml/h
Distance between nozzle and substrate	3 cm
Spray angle	90°
Spray nozzle diameter	0.2 mm
Deposition time	10 min

2.2.2. *XRD analysis*

Furthermore, films structural properties were determined using X-Ray diffraction (XRD), a relevant technique in the field of material characterization. Philips X'Pert system with Cu kα radiation (λ = 1.5406 Å) has been used. The obtained diffraction patterns were compared with 'ICDD' standards database [22] and all information of different crystallographic phases, relative abundance and preferred orientations have been extracted. From the width of the diffraction peak, the average grain size in the film can also be estimated. Films electrical characterization was performed using Hall effect measurement system, to determine carrier's concentration, mobility and electrical conductivity.

3. **Results and discussion**

3.1. *Deposition rate*

In Figure 2 we report the deposition rate (left y-axis) as well as the films thickness (right y-axis) variation as a function of the solution flow rate S_f. The deposition rate is estimated from the ratio of film thickness on the deposition time fixed at 10 min; their evolution is then similar. As can be seen, both parameters increase with increasing the solution flow rate where at a critical value S_f ≤10 ml/h, a peak takes place. After, a decrease of these parameters is observed with further increase of the solution flow rate and a minimum is observed at a second critical value S_f =15 ml/h. Growth onto the glass substrate (right at the beginning) should differ from growth onto the ZnO film itself. Besides this, as the film thickens several phenomena appear, such as nucleation, stress and relaxation, which should also produce variations in growth rate to some extent.

These results reveal that the films thickness is governed by the deposition rate and the control of the solution flow rate is crucial since it allows us deposition of thin films of desired thickness when using SPT. Note that in this particular case, the highest film growth rate was 42.43 nm/min for S_f =10 ml/h, whereas the lowest corresponding to S_f =15ml/h, is equal to 20.38 nm/min. This increase reduces the dissociation enthalpy and the chemical nature of the precursor. It was found [23] that the dissociation enthalpy of Zinc acetate is tenfold lower (0.1 kcal/mol) than the one of Zinc nitrate (10 kcal/mol). These values show that in deposition phase, acetate dissociates more easily than the nitrate. This explains the obtained high value of the growth rate of the films deposited with the acetate at the substrate temperature of 300 °C.

3.2. *X-Ray Diffraction Analysis*

X-Ray Diffraction (XRD) pattern of ZnO thin films deposited on glass substrates with various solution flow rates is shown in Figure 3. All the peaks correspond to those of standard ZnO (ICDD). In the XRD pattern (100), (101), (110) and (002) diffraction peaks are observed, showing the growth of ZnO crystallites along different directions. The crystallite size could be calculated by the Debye-Scherrer method from the FWHM (full width at half maximum) of the (100) reflection of ZnO [54, 55]:

$$D = \frac{0.94\lambda}{\beta \cos(\theta)} \qquad (1)$$

where D, λ, β and θ denote the crystallite size, the X-ray wavelength, FWHM, and the Bragg angle of (100) peak, respectively.
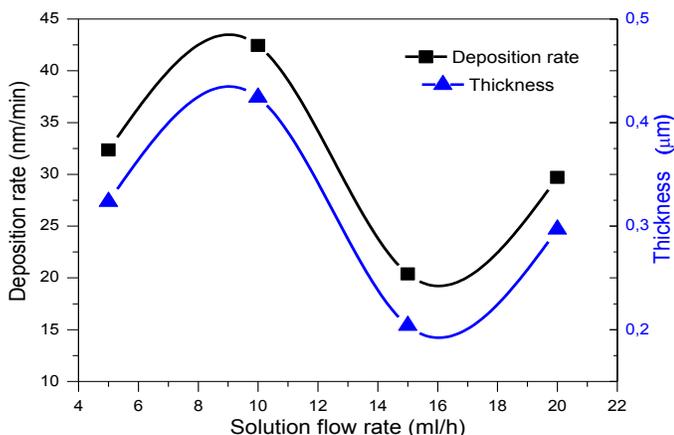
Figure 2: Deposition rate (left y-axis) and film thickness (right y-axis) dependence on solution flow rate. Symbols represent the experimental data and continuous curves correspond to a spline interpolate

The average uniform strain for the lattice along c-axis in the randomly oriented ZnO films deposited on glass substrate could be estimated from the lattice parameters using equation below [54, 55]:

$$\varepsilon = \frac{c - c_0}{c_0} \times 100\% \qquad (2)$$

where ε is the internal strain in Zn0 thin film, c the lattice constant of ZnO thin film and c_0 the lattice constant of bulk.

Calculated structural parameters are depicted in Table 2. Strong preferential growth is observed along (100) plane (orientated at 31.81° which is greater than the value 31.74° corresponding to ZnO powder) indicating that the thin films are oriented along the *c*-axis [24]. We interpret this orientation as a consequence of the confinement effect on developing grains following the model proposed by Van Der Drift [25]. According to this model, nucleations with various orientations can be formed at the initial stage of the deposition and each nucleus competes to grow but only nuclei having the fastest growth rate can survive. During the initial growth process of film, the grains oriented in the c-axis direction are developed, with suppressing growth of another grain, due to their rapid growing rate.

The variation of crystallite size and lattice strain as function of the solution flow rate S_f, are depicted in the same Figure 4. Here, we observe that from S_f =5 ml/h to S_f =15 ml/h, crystallite size increases (from 20.6 to 35.3 nm) as lattice strain decreases (from 0.61 to 0.36 %). The corresponding reduction of strain with increase of crystallite size during film growth, confirmed by the lattice parameter c = 0.5621 nm that is equal less than c_0 = 0.5633 nm (unconstrained layer), could be explained by rapid surface diffusion of material from the strained surface areas at the grain centers to the grain boundary regions [43] or by the gradual decrease of magnitude of strain with film thickness [44]. On the other hand, when the deposition is carried out in air, oxygen content and crystallinity

Table 2: Structural properties at different solution flow rates analyzed by XRD for plane [100]

S_f (ml/h)	$2\theta(°)$	FWHM	Lattice constant c (nm)	dislocation densities (10^{-3} nm^{-2})	crystallite size (nm)	Lattice strain (%)
5	31.87	0,4015	0.5611	2.35	20.6	0.61
10	31.58	0.2676	0.5660	1.04	30.9	0.41
15	31.81	0.2342	0.5621	0.80	35.3	0.36
20	31.73	0.2676	0.5635	1.04	30.9	0.41

increase as the speed of flow solution increases that is an element of this chemisorption. Oxygen excess recorded by the on-stoichiometry could be contained in the grain boundaries as discussed in ref [26]. In contrast, when the deposit is done under nitrogen or vacuum, the crystallinity varies in the same way as the oxygen content decreases. In this case, the increase in crystallinity can be achieved by the migration of oxygen atoms already present in the layer to a deficient site as shown in reference [27]. During rapid surface diffusion of a material, the amount of the solute reaching the surface of the substrate increases to form the film where the dominant electrostatic interactions between the solute atoms increase the probability of more solute to be gathered together to form a crystallite [5]. In the case where the films are deposited at a flow rate $S_f < 10$ ml/h, the small crystallites on the substrate are not able to grow into larger ones. Thus, the thinner films have smaller crystallites than the thicker ones, however as the film grows thicker, larger crystallites are formed via the gathering of more amount of solute [6]. Our results are consistent with data reported in refs [28, 29]. The decrease of crystallite size at $S_f > 15$ ml/h can be assigned to the degradation in the crystallinity induced by the structural defects and lattice distortion. XRD analysis shows that the film deposited at 15 ml/h presents optimal crystallization of ZnO hexagonal phase with a crystallite size of 35.3 nm, a lowest dislocation density equal to 0.8×10^{-3} nm^{-2} and a width at mid-height (FWHM, full width at half-maximum) of preferential peak with smallest value equal to 0.23°.
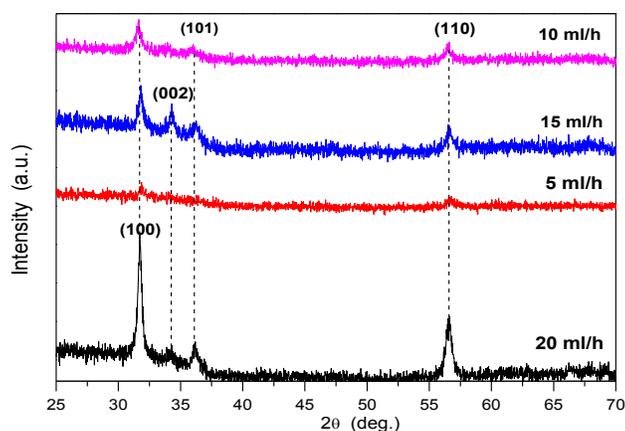
Figure 3: X-ray diffraction patterns of ZnO thin films deposited at different solution flow rates. of 5 ml/h, 10 ml/h, 15 ml/h and 20ml/h.

3.3. Optical properties
Measured transmission spectra at different spray rates are reported in Figure 5. As it can be seen, region of strong transparency is located between 380–1200 nm. All the samples exhibit an average optical transparency of about 94.89%, in the visible range, meanwhile the transparency is maximum (99.1%) at $S_f = 15$ ml/h. Previous reports

suggest that the emission of ZnO thin films in the blue-green band is strongly dependent on stoichiometry of the film [30]. Studenikin and al. [31] argued that oxygen vacancies and porosity of the film are the governing parameters of this emission.
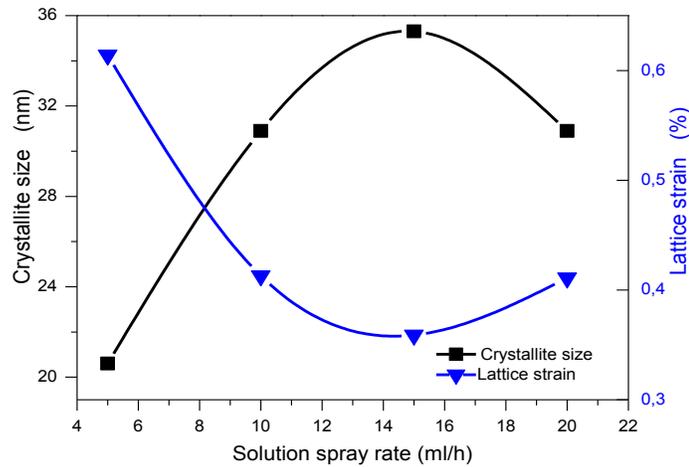
Figure 4: Crystallite size (square symbols) and Lattice strain (triangle symbols) of ZnO thin films versus solution flow rates.

The origin of the blue-green emission is due to transition from conduction band to the acceptor level corresponding to the antisite of oxygen. Interestingly, in the present work, the change in orientation as well as the introduction of antisite defects appears to be induced by the variation of spray rate. Through increasing the flow rate, we increase the quantity of zinc ions that would be available at the substrate surface to build the grains. Hydrogen interstitial insertion position may also be the cause of the increase of transmittance.

The abrupt fall in the transmission (as shown in the inset of Figure 5) for wavelengths below 380 nm (corresponding to photon energy > 3.1 eV) refers to the absorbance in ZnO. This corresponds to the region of the onset fundamental absorption in the layers due to the transition between the valence band and the conduction band.
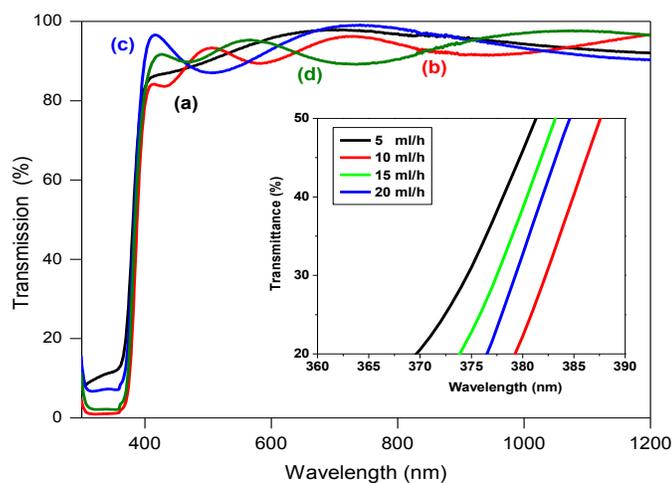
Figure 5: UV-Visible transmission spectrum of ZnO thin films deposited at different solution flow rates.
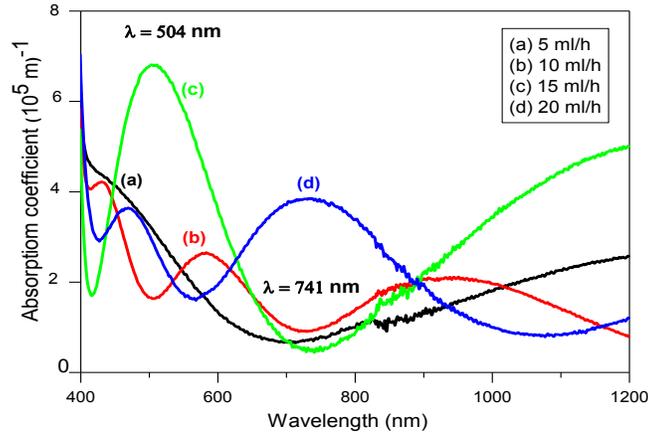
Figure 6: Absorption coefficient of ZnO thin films deposited at different solution flow rates.

The absorption coefficient (α) is computed from Beer-Lambert formula [58] reported in equation below:

$$\alpha d = -\log(T) \tag{3}$$

Measured and optical properties of ZnO thin films deposited at various S_f are depicted in Table 3, where the gap Eg is extrapolated from curve 7 and the Urbach energy E_U is computed using the equation 6.

Absorption coefficient (α) spectra of the deposited films are shown in Figure 6. A sharp decrease in α occurs near the band edge that indicates better crystallinity and lower defect density. We believe that more open structure allows the incorporation of impurities present on the surface or in the grain boundaries as stated in ref. [33]. Here it is quite obvious that the 'red transmission' centered at 741 nm is the most intense for the sample prepared at S_f =15 ml/h.

As it can be seen from Table 3, film thickness varies between 203.815 nm (S_f = 15 ml/h) and 424.382 nm (S_f = 10 ml/h) and the maximum of the transmission (Tmax) varies from 96.75% and 99.1%. The increase in the film thickness d is the leading parameter and main reason for the transmittance decrease. The thicker films consisting of more atoms and therefore more states avoid the absorption of the photons [32]. At a flow rate $10 \leq S_f \leq 15$ ml/h, d decreases as Tmax increases sharply; the optimum transparency is reached for S_f = 15 ml/h. At higher values of the flow rate, $S_f > 15$ml/h a reduction in transmittance is observed. This may be attributed to two facts, firstly to an increased scattering of photons by an increase in roughness of the surface morphology, secondly to poor crystallinity and defect density of increased ZnO film at higher S_f. The nature of the atmosphere during deposition has also a great influence on the composition of the thin layer of zinc oxide.
It is well known that direct transition across the band gap is feasible between valence and conduction band edges in the reciprocal space. Band gap energy (Eg) with direct transition can be calculated from the following relationship [34]:

$$\alpha h \nu = \left(B\left(h\nu - E_g\right)\right)^{1/2} \tag{4}$$

where B is a constant which takes a value between 107 and 108 m⁻¹, *h* is the Planck's constant, ν is the incident photon energy.

Typical plots of $(\alpha h\nu)^2$ versus $(h\nu)$ at different S_f are reported in Figure 7. Values of Eg are estimated from the x-axis intercept of the graph obtained by extrapolating linear portion of the exponential curve.

Table 3: Measured and computed optical proprieties of ZnO thin films deposited at various S_f

S_f (ml/h)	Thickness (nm)	% Tmax	E_g (eV)	E_U (meV)	α (10^{+4}m^{-1})
5	323.535	97.91	3.265	90.9	6.528
10	424.382	96.75	3.261	79.9	7.785
15	203.815	99.10	3.264	66.7	4.435
20	296.972	97.69	3.272	82.1	7.869
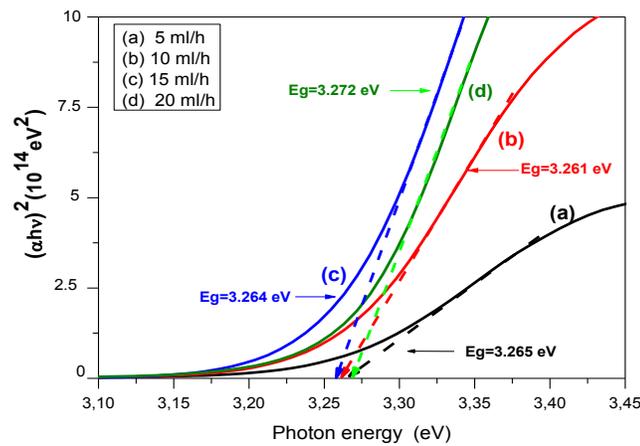
Figure 7: Typical variation of quantity $(\alpha h v)^2$ as a function of photon energy of ZnO thin films deposited at different solution flow rates.

As can be seen from Table 3, in all the cases, the gap energies obtained are less than the stoichiometric bulk value of ZnO [35]. This indicates a narrowing of the optical band gap and it might be interpreted as a Moss Burstein shift, which was ascribed to an increase of free carrier concentration, this leads to a downward shift of the Fermi level to below the band edge [52]. The dependence of the band gap upon S_f is depicted in the Figure 8. When $S_f \leq$ 10ml/h, Eg decreases from 3.265 to 3.261 eV with the increase of the thickness. Beyond S_f = 10ml/h, an increase of the optical band gap is observed - this can be attributed to the improvement of the crystallinity and the decrease of the strain. It is a well-known fact that two competing phenomena affect the band gap energy values with increasing the donor density, mainly in doped semiconductors [40]. The first one affects the decrease in the optical band gap of the ZnO films, which can be correlated to the increase in the carrier concentration (n) and decrease in the strain values. Hao and al. [36] have reported similar decrease of the band gap with the increase of the film thickness. The second phenomenon is related to the broadening of the band-gap energies of semiconductors due to Burstein–Moss effect [53]. The variation of the optical band gap supports and confirms the disorder in the films network. According to the Burstein–Moss effect, the increase in the Fermi level in the conduction band leads to the band gap energy broadening with increasing carrier concentration. Assuming parabolic energy bands and a spherical Fermi surface, the broadening of the optical band gap can be expressed as [37]:

$$E_g = E_0 + \Delta E_{BM} = E_0 + \frac{h^2}{8m^* \pi^2}(3\pi^2 n)^{2/3} \tag{5}$$

where n is the carrier concentration, m* is the reduced effective mass and E_0 is the band gap of undoped ZnO.

Urbach energy (E_U) is a parameter that includes effects of all possible defects and it describes the width of the localized states in the band gap [38]. Absorption coefficient near the band edge in the energy region of $h\nu < E_g$, empirically follows the exponential law [39]:

$$\alpha = \alpha_0 \exp(\frac{h\nu}{E_U}) \qquad\qquad (6)$$

where α_0 is a constant, E_U can be obtained from the slope of $\log(\alpha)$ versus photon energy ($h\nu$) plot.

The dependence of E_U upon S_f is also depicted in the same Figure 8. Firstly, we observe a decrease in E_U values from 90.9 meV to 66.7 meV as the film thickness increases from 323.535 nm to 424.382 nm indicating a reduction of the structural disorder and defects in the ZnO films. This result is in a good agreement with that is reported in refs. [40, 41]: Urbach energy E_U decreases from 114.4 meV to 61.4 meV as thickness increases from 632 nm to 1865 nm indicating the reduction of structural disorder and defects in the ZnO films. Also Tuzemen and al. reported in ref. [42] similar variation of the Urbach energy with the increase of thickness. Beyond the film thickness of 1865 nm, Urbach energy increases 101.6 meV.
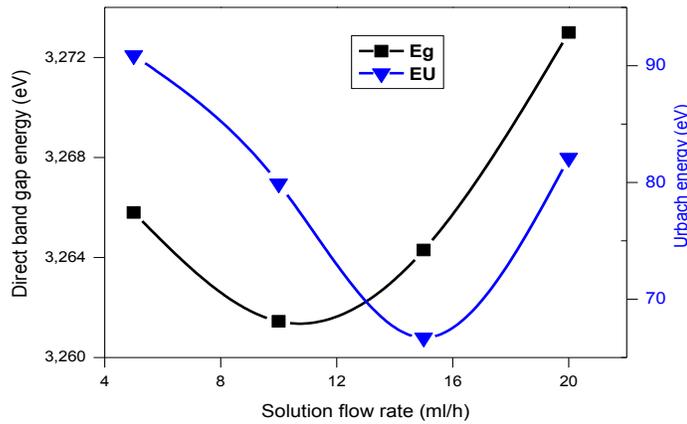
Figure 8: Band gap (square symbols) and Urbach energies (Triangles) of ZnO films versus solution flow rates.

3.4. *Electrical properties*

ZnO films deposited without any dopants show inherent n type conductivity. The Van Der Pauw technique [45] commonly used to measure the electrical resistivity has been applied to determine the dark resistivity of our prepared ZnO thin films. Electrical measurements were done after performing electrical contacts by using gold paint in the form of two end contacts with a length W =1 cm and sepa*rated by a distance L = 2.5 cm. Proceeding in a temperature variation in the range of 50 to 170 °C with a step value of 30 °C, the obtained results are depicted in Figure 9 where, the values of the resistance measurements (R) are plotted against the temperature T, at different flow rate S_f.

The electrical conductivity (σ) and consequently the mobility (μ) can be computed through the following equation:

$$\sigma = \frac{L}{wd} \frac{1}{R} \qquad\qquad (7)$$
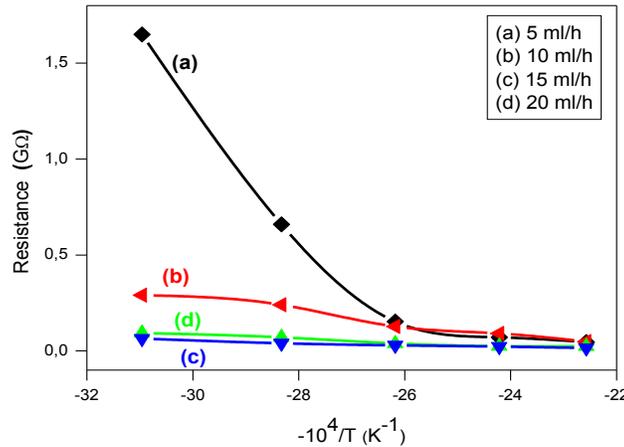
Figure 9: Resistance as a function of annealing temperature for ZnO films deposited at different solution flow rates.

The activation energy (Ea) of the thin films is related to the electrical conductivity [46] as shown by Eq.(8) and it can be estimated from the slope of the plot of log (σ) versus (-1/T).

$$\sigma = \sigma_0 \exp\left(- E_a / kT\right) \tag{8}$$

where k $=1.38\times10^{-23}$ J/T is the Boltzmann constant.

Furthermore, the carrier concentration (n) of the prepared ZnO thin films has been evaluated by using the following relation [6]:

$$E_U = 18.5\,10^{-12}(n/m^*\varepsilon)^{1/2} \qquad\qquad + \tag{9}$$

where, $\varepsilon = 8.5$ is the relative dielectric function of the ZnO and m* = 0.38.

Thus, by computing the values of (n) and (μ), the resistivity (ρ) can be calculated by using the relation [47]:

$$\rho = \frac{1}{ne\mu} \tag{10}$$

with e denoting the elementary charge.

The values of electrical parameters for the deposited ZnO thin films are given in Table 4. We report in the same Figure 10 the conductivity and the activation energy as function of the solution flow rate S_f. The variation of the carrier concentration and the mobility are shown both in Figure 11. Table 4 shows an increase in mobility from 1.98×10^{-5}cm^{2}V^{-1}s^{-1} to 13.9×10^{-5}cm^{2}V^{-1}s^{-1} (when the crystallite size ranged 20.6 nm-35.3 nm) as spray rate is increased from 5ml/h to 15 ml/h. Similarly M. Bouderbla and al report in ref. [48] the same behavior: the mobility increases from 10 cm^{2}V^{-1}s^{-1} to 22 cm^{2}V^{-1}s^{-1} respectively when crystallite size increases from 145 nm to 275 nm. Furthermore, larger crystallite size results in a lower density of the grain boundaries, which behave as traps for the free carriers and barriers for the carrier transport. With the improvement of the crystallinity, the concentration of the electrically active donor sites is improved [49]. As mentioned in ref. [50] a reduction of the ionized impurity scattering in the thicker films may be another reason of the high hall mobility.

Table 4: Measured and computed electrical proprieties of ZnO thin films deposited at various S_f.

S_f (ml/h)	Carrier concentration (10^{19} cm^{-3})	Mobility (10^{-5}cm^{2}V^{-1}s^{-1})	Resistivity ($10^3\Omega$ cm)	Sheet resistance (10^{10} $\Omega/\square$)	Φ_{TC} ($10^{-11}\Omega^{-1}$)
5	7.800	1.98	4.048	1.25	6.47
10	6.025	2.60	3.980	0.93	7.65
15	4.190	13.9	1.070	0.52	17.39
20	6.360	12.5	0.781	0.26	30.3
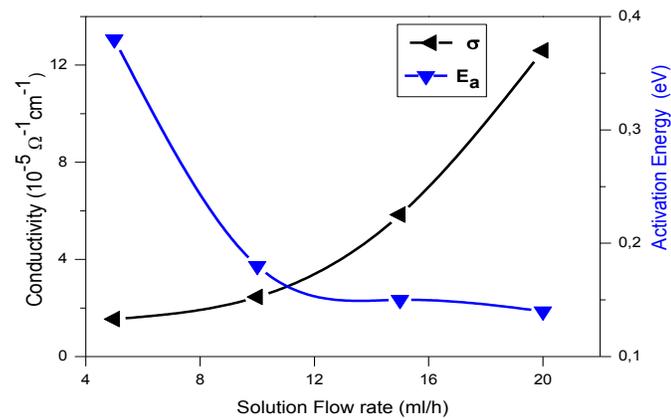
Figure 10: Conductivity at the dark and Energy of activation versus solution flow rates
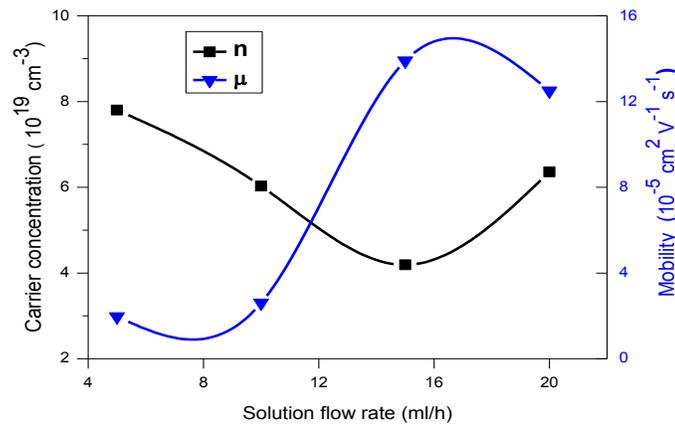
Figure 11: Carrier concentration and mobility versus solution flow rates.

The variation of the resistivity against the film thickness is depicted in Figure 12, where we observe a clear decrease with increasing the thickness and at the critical value of the solution flow rate $S_f \geq 15$ml/h, the electrical resistivity reaches its minimal value. The decrease in the resistivity of the films has been explained by displacement of the electrons by Zhang and al [51]. Generally electrical resistivity of ZnO thin films are ranged between 10^{-4} to 10^9 Ω cm [56]. In this work, at 300°C, the resistivity decreases from 4.048×10^3 to 0.781×10^3 Ω cm respectively when spray rate is increased from 5ml/h to 20 ml/h; similarly M. Kriisa reports in ref. [52] the

same behavior: the resistivity decreases from 6.3×10^{-2} to 3.7×10^{-3} Ω cm when spray rate is increased from 5ml/min to 3.3 ml/min.
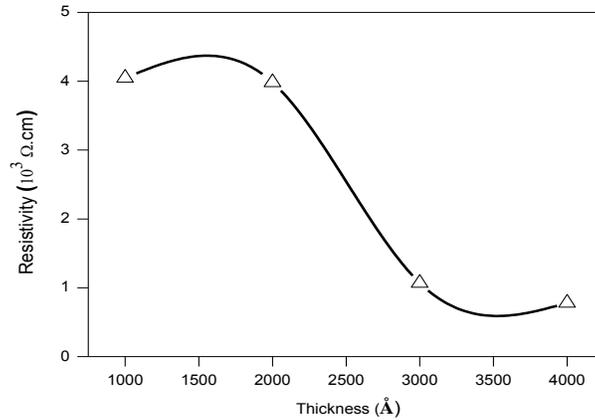
Figure 12: Plot of the resistivity as a function of the ZnO film thickness.

The figure of merit predicts transparent conducting oxide (TCO) properties by minimizing the trade-off between the electrical resistivity and the transparency. Excellent quality TCO film is associated with maximum value of the figure of merit. Φ_{TC} is calculating using the below formula [38]:

$$\phi_{TC} = \frac{(Transparency)^{10}}{Sheet\ resis\tan ce} \tag{11}$$

Finally, in Figure 13 we carried out the results corresponding to the figure of merit Φ_{TC} as well as the sheet resistance R_s as a function of the solution flow rate. It can be seen that Φ_{TC} increases and R_s decreases with increasing the solution flow rate. The required flow rate has to reach a critical value in order to achieve superior figure of merit, large conductivity and mobility that might enhance the light absorption due to the increased film thickness under such conditions.
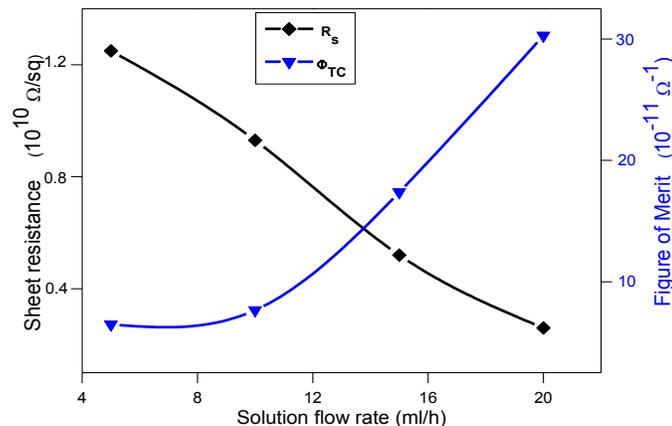
Figure 13: Plots of the figure of Merit Φ_{TC} and sheet resistance R_s versus S_f

Conclusions

In the present investigation, chemical spray deposition technique (SPT) was used to grow undoped ZnO thin films on glass substrates by varying the solution flow rates S_f (0.1 M zinc acetate). The influence of the spray deposition rate on the physical and structural properties investigated here was found to be significant. ZnO thin films deposited at S_f = 15 ml/h was highly transparent (99.1%) with a maximum dark electrical conductivity. Resistivity, carrier concentration and activation energy exhibit the lowest values (minimal). At the optimum spray rate a high value of the figure of merit Φ_{TC} = 17.4×10^{-11} Ω^{-1} was obtained suggesting that SPT provides a viable path towards nanocrystalline ZnO films suitable for applications in optoelectronic devices, such as window layers in solar cells, transparent conductive electrodes, flat panel display or window filter in photovoltaic devices.

References

1. Chen J., Chen J., Chen D., Zhou Y., Li W., Ren Y., Hu L., *Mater. Lett.* 117 (2014) 162.
2. Grara N. , Bouloudenine M., , Khaldi F. and al, *J. Mater. Environ. Sci.* 6 (9) (2015) 2596-2603.
3. Tominaga K., Murayama T., Mori I, Ushiro T., Nakabayashi T., *Thin Sol. Films* 386(2) (2001) 267.
4. Klenk R., Klaer J., Scheer R., Lux-Steiner M., Luck I., Meyer N., Ruhle U., *Thin Sol. Films* 480 (2005) 509.
5. Krunks M., Katerski A., Dedova T., Acik I.O., Mere A., *Sol. Ener. Mat. Sol. Cells* 92 (2008) 1016.
6. Hartnagel H.L., Dawar AL, Jain AK, Jagadish C *Semicond. Transp. Thin Films, IOP, Bristol institute of physics publishing,* (1995).
7. Suchea M., Christoulakis S., Katharakis M., Katharakis N., Kiriakidis G., *J. of Phys. Conf. Series* 10 (2005)147.
8. Choon-ho L., Do-Woo K., *Thin Solid Films* 546 (2013) 38.
9.   Hussein H.F., Shabeeb G. M., Hashim S. Sh., *J. Mater. Environ. Sci.* 2 (4) (2011) 423-426.
10. Skompska M., Zarebska K., *Electrochimica Acta* 127 (2014) 467.
11. Singh D., Singh S., Kumar U., Srinivasa R.S., Major S.S., *Thin Sol. F.* 555 (2014) 126.
12. Suwanboon S, Amornpitoksuk P, Bangrak P, Randorn, *Cer. Int.* 40 C (2014) 975.
13. Prajapati C.S., Kushwaha A., Sahay P.P., *Mat. Chem. and Phys.* 142 (2013) 276.
14. Lehrakia N. , Aida M.S., S. Abed S , Attaf N., Attaf A. , Poulain M. Current Applied Physics 12 (2012) 1283-1287.
15. Bacaksiz E., Parlak M., Tomakin M., ÖZcelik A., Karakız M., Altunbas M., *J. of Alloys and Compounds* 466 (2008) 447.
16. Ebothé J., Hichou El., Vautrot P., and Addou M., *Journal of Applied Physics*, 93, 1 (2003) 632–640.
17. Mahajan C.M., Takwale M.G., *Journal of Alloys and Compounds* 584 (2014) 128.
18. Rebien M., Henrion W., Bär M., Fischer C.H., *App. Phys. Lett*. 80 (2002) 3518.
19. Paraguay D.F., Estrada D.W., Acosta L.D.R., Andrade N.E., Yoshida M., *Thin Solid Films* 350 (1999) 192.
20. Vijayalakshmi K., Karthick K., Gopalakrishna D., *Cer. Inter.* 39 (1976) 4749.
21. Manifacier J.C., Gasiot J., Fillard J.P., *J. Phys. E: Sci. Instrum.* 9 (1976) 1002.
22. The International center for diffraction data, *http: // www.icdd.com* Accessed 20/Janvier/2015
23. Hafdallah A., *Dissertation University of Mentouri Constantine, Algeria* (2007).
24. Liu M., Wei X.Q., Zhang Z.G., Sun G., Chen C.S., Xue C.S., Zhuang H.Z., Man B.Y., *Appl Surf Sci.* 252 (2006) 4321.
25. Van Der Drift A., *Philips Research Reports* 22 (1967) 267.
26. Fang G.J., Li D., Yao B., *Thin Solid films* 418 (+2002) 156-162.
27. Moustagher A., *Dissertation Univer of Blaise P. Clermont-Ferrand II, France* (2004).
28. Dong B.Z., Fang G.J., Wang J.F., Guan W.J., Zhao X.Z., *Jour.of Appl.Phy.* 101(3) (2007)

29. Zhang D., He Y., Wang C.Z., *Optics and Laser Technology* 42(4) (2010) 556.
30. Vanheusden K., Seager C.H., Warren W.L., Tallant D.R., Voigt J.A., *Appl. Phys. Lett.* 68(3) (1996) 403.
31. Studenikin S.A., Golego N., Cocivera M., *J. Appl. Phys.* 83(4) (1998) 2104.
32. Ng-Cheng-Chin F., Roslin M., Gu Z.H., Fahidy T.Z., *J. Phys. D: Appl. Phys.* 31 (1998)71
33. Mahajan C.M., Takwale M.G., *Journal of Alloys and Compounds* 584 (2014) 128.
34. Urbach F., *Phys. Rev.* 92 (1953) 1324.
35. Ellmer K., Klein A., Rech B., *Springer Series in Materials Science* (2008) 80.
36. Hao X., Ma J., Zhang D., Yang T., Ma H., Yang Y., Cheng C., *Applied Surface Science* 183(1/2) (2001) 137.
37. Cao L., Zhu L.P., Chen W.F., Ye Z.Z., *Optical Materials* 35(6) (2013) 1293.
38. Caglar M., Ilican S., Caglar Y., *Thin Solid Films* 517(17) (2009) 5023.
39. Tauc J., *Amorp. and Liq. Semicond.. Plenum Press, London and New York* (1974).
40. Swapna R., Ashok M., Muralidharan G., Kumar M.C.S., *J. of Anal. and App. Pyro.* 102 (2013) 68-75.
41. Benramache S., Chabane F., Benhaoua B. , Lemmadi F.Z., *Journal of Semiconductors* 34 (2) (2013) 1-4
42. Tuzemen E.S., Eker S., Kavak H., Esen R., *Applied Surface Science* 255 (2009) 6195.
43. Chaudhari P., *Journal of Vacuum Science and Technology* 9 (1972) 520.
44. Abermann R., Koch R., *Thin Solid Films* 142 (1986) 65.
45. Van Der Pauw L.J., Philips Research Reports 13 (1958) 1.
46. Wu S.P., Zhao Q.Y., Zheng L.Q., Ding X.H., *Solid State Sciences* 13(3) (2011) 548.
47. Igasaki Y., Saito H., *Thin Solid Films* 199 (1991) 223.
48. Bouderbla M., Hamzaoui S., Adnane M., Sahraoui T, Zerdali M., *Thin Solid Films* 517 (2009) 1572-1576
49. Jung Y.S., Seo J.Y., Lee D.W., Jeon D.Y., *Thin Solid Films* 445 (1) (2003) 63.
50. Fortunato E., Assunçäo V., Goncalves A., Marques A., Águas H., Pereira L., Ferreira I., Vilarinho P.,
     Martins R., *Thin Solid Films* 451/452 (2004) 443.
51. Zhang D H, Yang T L, Ma J, and al. *Appl Surf Sci*, 158(1) (2000) 43. •
52. Kriisa M., Krunks M., Kärber E., Kukk et al, *Journal of Nanomat.*2013 (2013), Article ID 423632, 9.
53. Miloslavskii V. K., Pogrebniak P. S.,   *physica status solidi (b)* 51(2) (1972) K99–K102.
54. Cullity B.D, *Elements of X-Ray Diffraction*, Addison-Wesley Publishing Co, (1956) 98–99.
55. H.P. Klung, L.E. Alexander, *X-ray Diffraction Procedures for Polycrystalline and Amorphous Materials,*
     second ed., Wiley, New York, (1974).
56. Asmar R.Al, Ferblantier G. Mailly F., Gall-Borrut P., Foucaran A., *Thin Solid Films* 473 (2005) 49-53.
57. Ynineb F., Hafdallaha A , Aida M.S., Attaf N et al *Materials Sc. in Semicond. Proc.* 16 (2013) 2021–2027
58. E.D. Palik: *Handbook of optical constants of solids.* Elsevier (1998).

(2016); http://www.jmaterenvironsci.com/